



<b>Publication Year</b>	2018
<b>Acceptance in OA @INAF</b>	2020-10-15T14:05:12Z
<b>Title</b>	X-Ray Photo-desorption of H <sub>2</sub> O:CO:NH <sub>3</sub> Circumstellar Ice Analogs: Gas-phase Enrichment
<b>Authors</b>	JIMENEZ ESCOBAR, Antonio; CIARAVELLA, Angela; CECCHI PESTELLINI, Cesare; Huang, C.-H.; Sie, N.-E.; et al.
<b>DOI</b>	10.3847/1538-4357/aae711
<b>Handle</b>	<a href="http://hdl.handle.net/20.500.12386/27848">http://hdl.handle.net/20.500.12386/27848</a>
<b>Journal</b>	THE ASTROPHYSICAL JOURNAL
<b>Number</b>	868



# X-Ray Photo-desorption of H<sub>2</sub>O:CO:NH<sub>3</sub> Circumstellar Ice Analogs: Gas-phase Enrichment

A. Jiménez-Escobar<sup>1</sup> , A. Ciaravella<sup>1</sup> , C. Cecchi-Pestellini<sup>1</sup> , C.-H. Huang<sup>2</sup>, N.-E. Sie<sup>2</sup>, Y.-J. Chen<sup>2</sup> , and G. M. Muñoz Caro<sup>3</sup>

<sup>1</sup> INAF—Osservatorio Astronomico di Palermo, P.zza Parlamento 1, I-90134 Palermo, Italy

<sup>2</sup> Department of Physics, National Central University, Jhongli City, Taoyuan County 32054, Taiwan; [asperchen@phy.ncu.edu.tw](mailto:asperchen@phy.ncu.edu.tw)

<sup>3</sup> Centro de Astrobiología (INTA-CSIC), Carretera de Ajalvir, km 4, Torrejón de Ardoz, E-28850 Madrid, Spain

Received 2018 July 26; revised 2018 September 30; accepted 2018 October 6; published 2018 November 21

## Abstract

We study the photo-desorption occurring in H<sub>2</sub>O:CO:NH<sub>3</sub> ice mixtures irradiated with monochromatic (550 and 900 eV) and broadband (250–1250 eV) soft X-rays generated at the National Synchrotron Radiation Research Center (Hsinchu, Taiwan). We detect many masses photo-desorbing, from atomic hydrogen ( $m/z = 1$ ) to complex species with  $m/z = 69$  (e.g., C<sub>3</sub>H<sub>3</sub>NO, C<sub>4</sub>H<sub>5</sub>O, C<sub>4</sub>H<sub>7</sub>N), supporting the enrichment of the gas phase. At low numbers of absorbed photons, substrate-mediated, exciton-promoted desorption dominates the photo-desorption yield, inducing the release of weakly bound (to the surface of the ice) species; as the number of weakly bound species declines, the photo-desorption yield decreases about one order of magnitude, until porosity effects, reducing the surface/volume ratio, produce a further drop of the yield. We derive an upper limit to the CO photo-desorption yield, which in our experiments varies from 1.4 to 0.007 molecules photon<sup>-1</sup> in the range  $\sim 10^{15}$ – $10^{20}$  absorbed photons cm<sup>-2</sup>. We apply these findings to a protoplanetary disk model irradiated by a central T Tauri star.

*Key words:* ISM: molecules – X-rays: ISM – astrochemistry

## 1. Introduction

Interstellar ice mantles, formed mainly by H<sub>2</sub>O, may also contain a variety of C- and N-bearing molecules such as CO<sub>2</sub>, CO, CH<sub>3</sub>OH, and NH<sub>3</sub> (Boogert et al. 2015). Laboratory simulations indicate that energetic processing of these ices can produce a large number of complex organic compounds, which can include molecules of biological interest such as alcohols, quinones, esters, amino acids (e.g., Muñoz Caro et al. 2002), and sugars (Meinert et al. 2016). Recently, during the *Rosetta* mission, many complex organic molecules such as acetaldehyde (CH<sub>3</sub>CHO) and formamide (NH<sub>2</sub>CHO) have been detected in the environment of comet 67P/Churyumov–Gerasimenko (Goesmann et al. 2015). In the accompanying coma, mass spectroscopy measurements are compatible with biologically active compounds, such as glycine (Altwegg et al. 2016), or glycine structural isomers (Oba et al. 2016).

Gas phase observations have detected a large number of molecular species in cold clouds in which the temperature is around 10 K. Thus, non-thermal desorption from dust surfaces are crucial for our understanding of the chemical evolution of such regions. In addition to photon-induced desorption, cosmic-ray bombardment of icy dust is expected to drive non-thermal desorption. Because of the low penetration depth of ultraviolet photons, only the outskirts of dense clouds are exposed to ultraviolet; well inside the cloud, ice mantles are processed by the secondary ultraviolet field generated by cosmic-ray excitation of molecular hydrogen. The direct impact of cosmic rays on icy dust is expected to desorb volatiles significantly (Dartois et al. 2015), while X-rays may also contribute to the desorption of ice mantles in circumstellar regions around young stars. Release of chemical energy was also proposed as a non-thermal desorption mechanism (e.g., Garrod et al. 2007). Photochemical desorption or photo-chemidesorption is the immediate desorption of molecules triggered by a photon after their formation on the ice surface, which leads to a constant desorption rate

(Martín-Doménech et al. 2015). Ice explosions could be driven by chemical energy, released sporadically when the growing population of radicals in the ices spontaneously associate (e.g., Rawlings et al. 2013).

Ultraviolet radiation can induce desorption from the surface through two principal mechanisms. The first, desorption induced by electronic transitions (DIET; e.g., Martín-Doménech et al. 2015), is initiated by absorption in the first layers of the ice, exciting molecules to high-lying electronic states. The excitation energy is then dissipated to the surface of the ice by transferring to neighboring molecules. The transmitted energy is high enough to overcome intermolecular interactions, eventually ejecting the molecule into the gas phase (Öberg et al. 2007; Muñoz Caro et al. 2010; Fayolle et al. 2011, 2013; Martín-Doménech et al. 2015). The second mechanism is photo-chemidesorption (Martín-Doménech et al. 2015, 2016).

X-rays are absorbed deep inside the ice matrix, leading to the fragmentation of molecules. In general, this occurs through the ionization or excitation of an inner-shell electron, followed by either normal or resonant Auger decays, with the normal Auger decay active above the ionization threshold. The injection of energetic photoelectrons produces multiple ionization events, generating a secondary electron cascade that dominates the chemistry (e.g., Jiménez-Escobar et al. 2016). X-ray-induced photo-desorption may be caused by three channels: (1) photon-stimulated desorption (PSD) resulting from the fragmentation of surface molecules after their own core excitation (Parent et al. 2002); (2) Auger-stimulated ion desorption where, after core electron excitation, Auger transitions cause the formation of two holes in the valence orbital, with final desorption of the resulting ion after relaxation (Sekitani et al. 1997); (3) X-ray-induced electron-stimulated desorption, in which electrons emitted from the bulk can induce non-resonant fragmentation of the surface molecules by, e.g., interband transition, and dissociative electron attachment. In that case, the fragmentation is simply proportional to the electron yield (Parent et al. 2002).

**Table 1**  
Irradiation Experiments

Exp.	Energy (keV)	N(H <sub>2</sub> O) (cm <sup>-2</sup> )	N(CO) (cm <sup>-2</sup> )	N(NH <sub>3</sub> ) (cm <sup>-2</sup> )	Photon rate (photon s <sup>-1</sup> )	Tot. imp. ph. (photons)	Tot. abs. ph. (photons)	Tot. abs. E. (eV)
M5	0.55	$4.34 \times 10^{17}$	$3.57 \times 10^{17}$	$2.95 \times 10^{17}$	$9.02 \times 10^{12}$	$6.49 \times 10^{16}$	$3.02 \times 10^{16}$	$1.66 \times 10^{19}$
M9	0.90	$4.52 \times 10^{17}$	$3.56 \times 10^{17}$	$2.70 \times 10^{17}$	$7.75 \times 10^{12}$	$5.58 \times 10^{16}$	$9.07 \times 10^{15}$	$8.13 \times 10^{18}$
BBw	0.25–1.2	$4.42 \times 10^{17}$	$3.57 \times 10^{17}$	$2.79 \times 10^{17}$	$6.62 \times 10^{13}$	$4.77 \times 10^{17}$	$1.14 \times 10^{17}$	$7.56 \times 10^{19}$
BBs	0.25–1.2	$4.15 \times 10^{17}$	$3.54 \times 10^{17}$	$2.72 \times 10^{17}$	$6.03 \times 10^{15}$	$4.34 \times 10^{19}$	$1.01 \times 10^{19}$	$6.67 \times 10^{21}$

Non-thermal desorption of molecular ices may be mediated by excitons, in terms of excitation of a substrate–adsorbate complex and the Menzel–Gomer–Redhead mechanism (McCoustra & Throer 2018).

In this work we study the photo-desorption occurring in H<sub>2</sub>O:CO:NH<sub>3</sub> ice mixtures irradiated with monochromatic (550 and 900 eV) and broadband (250–1250 eV) soft X-rays from the BL08B beamline at the National Synchrotron Radiation Research Center (NSRRC, Hsinchu, Taiwan). Other effects of soft X-ray irradiation, i.e., formation of volatile photo-products and the organic residue that remains at room temperature, are discussed in a companion paper (Ciaravella et al. 2018).

The experiments are described in Section 2; photo-desorbing species induced by X-rays are listed and discussed in Section 3. The dependence of photo-desorption yield on the physical conditions during the experiment (e.g., the photon rate) is presented in Section 4. Results are discussed in Section 5. Conclusions and astrophysical implications of X-ray-induced photo-desorption are given in the last section.

## 2. Experiments

The experiments were carried out in the Interstellar Photo-process System (IPS), an ultrahigh vacuum chamber of base pressure  $1.3 \times 10^{-10}$  mbar. A Fourier transform infrared (FTIR) ABB FTLA-2000-104 spectrometer equipped with a mercury–cadmium–telluride infrared detector and a quadrupole mass spectrometer (QMS) in the range 1–200 amu (0.5 amu resolution) were used to monitor the ice and the composition of the gas in the chamber. The gas line system, baked out at 120 °C to eliminate organic and water contamination, reaches a minimum pressure of  $1.3 \times 10^{-7}$  mbar before preparing the gas mixture for the experiments. For a detailed description of the IPS facility we refer to the work of Chen et al. (2014).

We irradiated an ice mixture of H<sub>2</sub>O+CO+NH<sub>3</sub> (1.5:1.3:1 in ratio) at 15 K for a total of 120 min. We chose a mixture rich in CO and NH<sub>3</sub> to maximize the photo-product abundances that are otherwise difficult to detect. As X-ray source we used the spherical grating monochromator beamline BL08B at the NSRRC, covering photon energies from 250 to 1250 eV. The spectrum is the same as in Ciaravella et al. (2018). We irradiated over the whole available band (broadband BB) at two different fluxes, and monochromatic photons of 550 (M5) and 900 (M9) eV. Before and after irradiation, infrared spectra were collected with a resolution of 1, 2, and 4 cm<sup>-1</sup>. During the experiment, the irradiation was stopped several times ( $\Delta t = 0.5, 1, 5, 10, 20, 40, 60, 80, 100,$  and 120 min), when infrared spectra were taken with a resolution of 2 cm<sup>-1</sup>. At the end of the irradiation, the ice was heated up to room temperature at a rate of 2 K min<sup>-1</sup>. During the warm-up, infrared spectra were acquired every 10 K with a resolution of 4 cm<sup>-1</sup>.

The set of experiments is reported in Table 1, in which for each experiment we also report the employed X-ray energies, initial H<sub>2</sub>O, CO, and NH<sub>3</sub> column densities, photon rate, the total number of impinging and absorbed photons in the ice, and the total absorbed energy by the sample in each experiment. The X-ray flux impinging on the ice decreases exponentially as it propagates inside it. To compute this decrease we exploit the X-ray database tool (<http://henke.lbl.gov>), which includes photo-absorption, scattering, and transmission coefficients by Henke et al. (1993). The photon flux was derived taking into account the size of the X-ray spot,  $A_X = 0.08$  cm<sup>2</sup>.

The column density values reported in Table 1 are obtained using the following band strengths:  $A(\text{H}_2\text{O}) = 1.2 \times 10^{-17}$  cm molecule<sup>-1</sup> (Gerakines et al. 1995) at 1660 cm<sup>-1</sup>,  $A(\text{CO}) = 1.1 \times 10^{-17}$  cm molecule<sup>-1</sup> (Jiang et al. 1975) at 2142 cm<sup>-1</sup>, and  $A(\text{NH}_3) = 1.7 \times 10^{-17}$  cm molecule<sup>-1</sup> (Sandford & Allamandola 1993) at 1112 cm<sup>-1</sup>. The total column density of the mixture is computed as the sum of the column densities of the components,  $N_T = N_{\text{H}_2\text{O}} + N_{\text{CO}} + N_{\text{NH}_3}$ .

We plot in Figure 1 the infrared spectra of the BBs ice mixture before and after irradiation of 120 min, equivalent to a total number of impinging photons of  $4.34 \times 10^{19}$  (see Table 1). Irradiation with different photon rates leads to the same photo-products. In this paper, only the photo-desorbed species are reported. A complete list of the products is in Table 1 of Ciaravella et al. (2018).

## 3. Photo-desorbing Fragments Induced by X-Rays

In this work we study the photo-desorption arising during the X-ray irradiation of the ice sample, exploring different radiation energies and fluxes. The assumed fluxes cover about three orders of magnitude.

X-rays induce photo-desorption of the ice mixture components (parent molecules) as well as of the products. Irradiation with the weakest fluxes (M5 and M9) produced only a faint desorption of mass 28. In the BBw experiment, desorptions of masses 1, 2, 12, 17, 18, 28, 30, 32, and 44 were observed, while the more intense photo-desorption and the largest mass inventory were detected using the strongest flux (BBs). For this reason, we mainly focus on the BBs experiment. Figure 2 shows all the masses photo-desorbing during this experiment.

All masses show 10 desorption peaks, as many as the number of radiation steps. The intensity of the desorption peaks decreases rapidly with the irradiation time. In Table 2 we list the fragmentation pattern of parent molecules produced by electron impact ionization in the QMS. In Figure 3 we plot for each mass the total ion current after each radiation step against the irradiation time. The total ion current is computed as sum of all accumulated desorption peaks up to the selected radiation step. The signal of the QMS spectrum extends over more than three orders of magnitude, and is dominated by  $m/z = 2, 18,$  and 28 over any other species.

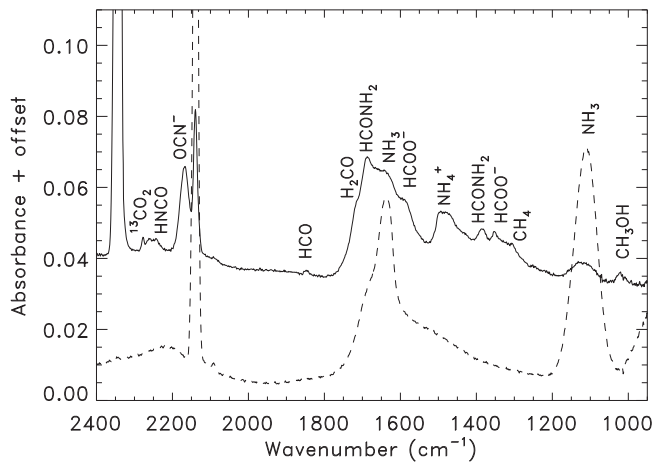


**Figure 1.** Infrared spectra of the BBs ice sample before (dashed line) and after (solid line) irradiation. The irradiated spectrum has been shifted for clarity.

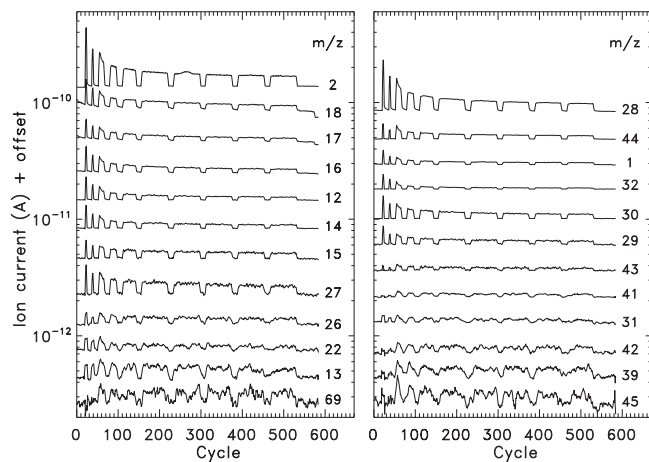


**Figure 2.** Ion current for the masses detected by a quadrupole mass spectrometer during the BBs experiment as a function of the scanning time measured in cycles (one cycle is about 19 s). The curves have been shifted for clarity.

**Table 2**  
Fragmentation of the Parent Molecules

Fragments ( $m/z$ )	Species		
	CO	H <sub>2</sub> O	NH <sub>3</sub>
12	0.04414	...	...
14	...	...	0.022
15	...	...	0.071
16	0.01458	0.021	0.8948
17	...	0.259	1
18	...	1	...
19	...	0.0011	...
28	1	...	...

In Table 3 are listed the molecular formulae of the detected masses. Since the QMS is much more sensitive than the FTIR spectrometer, we cannot exclude the contribution to each mass from species that are not clearly detected in the infrared spectra. In the following we discuss the major contributor for each mass.

1.  $m/z=28$ . This mass is directly associated with CO and N<sub>2</sub>. The contribution of CO<sub>2</sub> to mass 28 is less than 3%

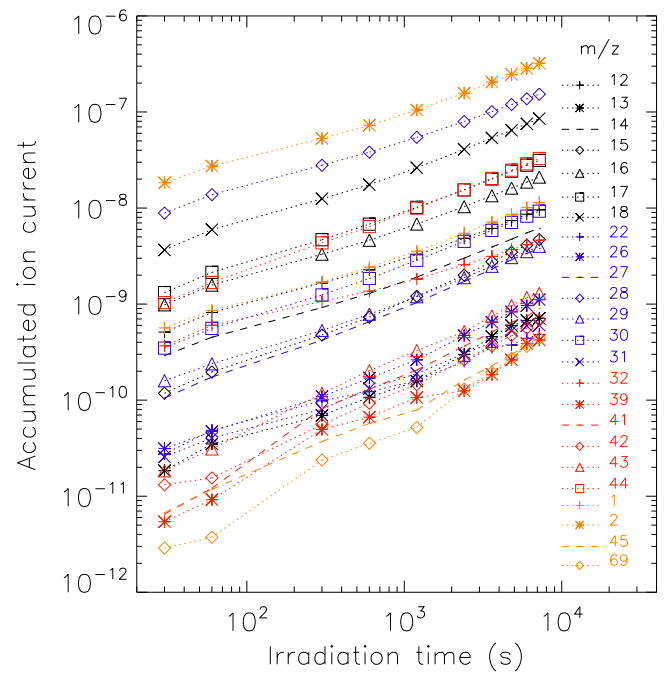


**Figure 3.** Accumulated quadrupole mass spectrometer signal as a function of the irradiation time for the photo-desorbing species detected during irradiation in the BBs experiment (see Table 1).

**Table 3**  
Fragments Detected by QMS During Irradiation

$m/z$ (amu)	Fragments
1	H
2	H <sub>2</sub>
12	C
13	CH
14	N, CH <sub>2</sub>
15	HN, CH <sub>3</sub>
16	O, NH <sub>2</sub> , CH <sub>4</sub>
17	HO, NH <sub>3</sub>
18	H <sub>2</sub> O
22	CO <sub>2</sub> <sup>+</sup>
26	CN, C <sub>2</sub> H <sub>2</sub>
27	HCN
28	CO, N <sub>2</sub>
29	HCO, <sup>13</sup> CO, <sup>15</sup> NN, HN <sub>2</sub> , CH <sub>3</sub> N
30	H <sub>2</sub> CO, H <sub>2</sub> N <sub>2</sub> , CH <sub>4</sub> N, C <sub>2</sub> H <sub>6</sub> , NO
31	CH <sub>3</sub> O, CH <sub>5</sub> N, HNO
32	O <sub>2</sub> , CH <sub>3</sub> OH, H <sub>2</sub> NO, H <sub>4</sub> N <sub>2</sub>
39	C <sub>2</sub> HN, C <sub>3</sub> H <sub>3</sub>
41	CH <sub>3</sub> CN, C <sub>2</sub> HO, CHN <sub>2</sub> , C <sub>2</sub> H <sub>3</sub> N, C <sub>3</sub> H <sub>5</sub>
42	NCO, N <sub>3</sub> , C <sub>2</sub> H <sub>2</sub> O, CH <sub>2</sub> N <sub>2</sub> , C <sub>3</sub> H <sub>6</sub>
43	HNCO, C <sub>2</sub> H <sub>3</sub> O, C <sub>2</sub> H <sub>5</sub> N, C <sub>3</sub> H <sub>7</sub>
44	CO <sub>2</sub> , N <sub>2</sub> O, CH <sub>2</sub> NO, C <sub>2</sub> H <sub>4</sub> O, CH <sub>4</sub> N <sub>2</sub> , C <sub>3</sub> H <sub>8</sub>
45	<sup>13</sup> CO <sub>2</sub> , C <sub>2</sub> H <sub>5</sub> N, CH <sub>3</sub> NO, CO <sub>2</sub> H
69	C <sub>3</sub> H <sub>3</sub> NO, C <sub>4</sub> H <sub>5</sub> O, C <sub>4</sub> H <sub>7</sub> N

since mass 44 is around five times lower than  $m/z=28$  and the relative intensity of  $m/z=28$  in the CO<sub>2</sub> mass spectrum is 12%. The main fragment of N<sub>2</sub> is atomic N ( $m/z=14$ ) with a fragmentation ratio of 14% with respect to N<sub>2</sub> ([www.nist.gov](http://www.nist.gov)); assuming that mass 14 comes exclusively from N<sub>2</sub>, we conclude that the

- contribution of  $N_2$  to  $m/z=28$  is at most 25%. Thus,  $m/z=28$  mostly comes from CO in the ice mixture.
2.  $m/z=18$ . This mass is assigned to  $H_2O$  which is the third most intense signal after  $m/z=2$  and 28 during irradiation.
  3.  $m/z=17$ . OH is one of the carriers of this mass with an abundance of  $\sim 26\%$  with respect to water; however, this is not enough to justify the detected intensity. The ratio of  $m/z=18$  and 17 is  $\sim 0.45$ , a value much higher than that given for  $H_2O$  in Table 2. Another main contributor to this mass is  $NH_3$ , a parent molecule.
  4.  $m/z=44$  and 22.  $CO_2$  is the most abundant product of the irradiated ice, and the carrier of  $m/z=44$ . It also contributes to  $m/z=12$ , 16, 28, and 32. The mass 22 can be justified by a double ionization of  $CO_2$  in the QMS with a ratio of 1.6% with respect to  $CO_2$ .  $N_2O$ , a possible carrier for the infrared-blended feature between 2200 and 2300  $cm^{-1}$  (see Pilling et al. 2010), could also contribute to mass 44.
  5.  $m/z=43$  and 42. HNCO contributes to the infrared features in the 2300–2200  $cm^{-1}$  range. Photo-desorption of this species can explain the signal of  $m/z=43$  and 42 amu, HNCO and OCN respectively (Jiménez-Escobar et al. 2014). Photo-desorption of these fragments have also been found during ultraviolet irradiation (Chen et al. 2011).
  6.  $m/z=41$  and 39. Mass 41 has not been detected during ultraviolet irradiation of ice analogues (Chen et al. 2011). One possible candidate is  $CH_3CN$  (acetonitrile) which also contributes to mass fragment 39 and 40 amu. However, the intensity of  $m/z=40$  has not been observed (it is at the noise level). Acetonitrile has not been clearly detected in the infrared spectra. Mencos & Krim (2016) found that  $CH_3CN$  has a strong absorption at 2260  $cm^{-1}$  which overlaps with the HNCO and  $^{13}CO_2$  features. The QMS is more sensitive than the FTIR, allowing the detection of trace compounds. Alternatively, the  $m/z=39$  can be assigned to CHCN (cyanomethylene) which could also contribute to masses 13 and 26 amu. According to Maier et al. (1988) CHCN has a strong feature at 1735  $cm^{-1}$  which could be blended with the features around the peak at 1688  $cm^{-1}$ .
  7.  $m/z=32$ .  $O_2$  production can explain this mass. Its fragmentation also contributes to mass 16 (O). The photo-desorption of  $CH_3OH$  could also increase  $m/z=32$ . However, direct photo-desorption of  $CH_3OH$  (from pure methanol ices) in the ultraviolet (Cruz-Díaz et al. 2016), and X-rays (Y.-J. Chen, private communication) is negligible. On the other hand, in ice mixture conditions,  $CH_3OH$  could co-desorb with other molecules. However, the main signal of  $CH_3OH$  measured by the QMS is  $m/z=31$ , whose intensity is significantly lower than  $m/z=32$ , while it should be the opposite (the relative intensity of mass 32 with respect to mass 31 is 0.69). Thus, the methanol contribution to  $m/z=32$  is very small.
  8.  $m/z=31$ , 30, and 29. Direct  $CH_2OH$  and  $CH_3O$  fragments could contribute to mass 31. Direct photo-desorption of  $H_2CO$  ( $m/z=30$ ) cannot explain the intensity of mass 29 (HCO). The contribution of CO to mass 29 ( $^{13}CO$ ) is 1.2% smaller than the 10% found in our experiments. Thus, direct photo-desorption of HCO

should take place. This species is also seen in the infrared spectra at 1848  $cm^{-1}$ . Nevertheless, more exotic compounds such as  $CH_2NH$  could be involved.

9.  $m/z=26$  and 27. These masses can be assigned to CN and HCN, respectively. Nevertheless, no HCN features have been detected in the infrared spectrum, probably due to the high reactivity of this species in the ice matrix. The detection of neutral reactive species suggests a non-dissociative photo-desorption mechanism.
10.  $m/z=14$  and 15. These masses are assigned to N and NH respectively. Mass 14 could come from  $N_2$ . However, mass 14, similar to mass 15, can also come from direct photo-desorption of  $NH_3$  fragments formed in the ice.
11.  $m/z=12$  and 16. CO,  $H_2O$ ,  $NH_3$  and  $CO_2$  contribute to this signal. Carbon monoxide and dioxide participate in  $m/z=12$ . However, a plethora of more complex products formed during irradiation could provide these fragments after ionization in the QMS.
12.  $m/z=45$ . The  $CO_2$  could contribute to mass 45 due to  $^{13}CO_2$  which has a natural abundance of 1.1% with respect to  $^{12}CO_2$ . From Figure 3 we can deduce a ratio  $(m/z=45)/(m/z=44) \approx 1.2\%$ , similar to the natural abundance. However, other compounds may contribute, such as  $NH_2CHO$  detected in the infrared spectrum (see Figure 1).
13.  $m/z=69$ . Although noisy, this mass has been detected, suggesting photo-desorption of species with relatively high masses. Possible fragments are  $C_3H_3NO$ ,  $C_4H_5O$ , or  $C_4H_7N$ . No signal has been found during the first minute of irradiation, supporting a complex reaction processes in which precursors have to be formed.

A list of all the detected masses, and their possible assignments, are reported in Table 3.

#### 4. Photo-desorption Yield

In the analysis of X-ray-induced desorption, we use mass 28 as a reference, because this mass is the only detection common to all the experiments. The corresponding  $m/z=28$  mass spectra are reported in Figure 4. It is evident that the intensity of the ion current grows with the photon rate, and decreases with irradiation time. As a consequence, in the experiments subjected to the lowest photon rates, the ion current intensity falls rapidly at the noise level.

To quantify the amount of species released in the photo-desorption events we show in Figure 5 the accumulated QMS ion current  $IC$  of mass 28 (see Figure 4) as a function of the absorbed photons for all the experiments described in Table 1. We find that in a photon rate range covering three orders of magnitude, the accumulated ion current increases with the number of absorbed photons,  $F_{abs}$ . This evidence is in contrast with the general trend of photo-reaction yields produced by X-ray irradiation in ices, in which a strong dependence on the flux has been observed in many experiments involving, e.g.,  $CH_3OH$  (Chen et al. 2013), CO (Ciaravella et al. 2016), and  $H_2O$ –CO mixtures (Jiménez-Escobar et al. 2016). Figure 5 also suggests that the photo-desorption yield is larger during the early stages of the experiments, decreasing with irradiation time, as is actually confirmed by the data reported in Figure 6. We fit the photo-desorption yield of CO exploiting a

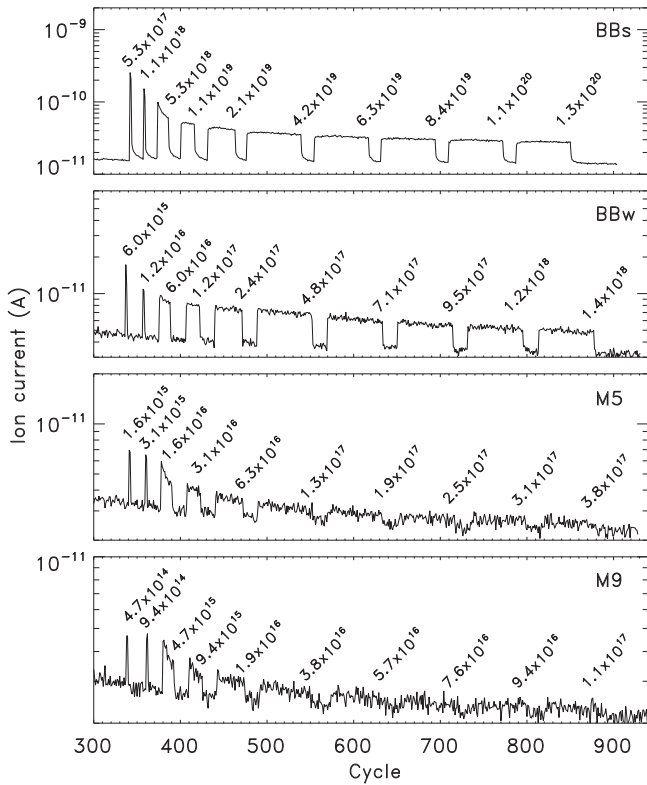


**Figure 4.** Ion current for  $m/z=28$  detected by the QMS during the experiments reported in Table 1. The impinging photon rate decreases from top to bottom. Labels indicate the total absorbed photons at the end of each irradiation step.

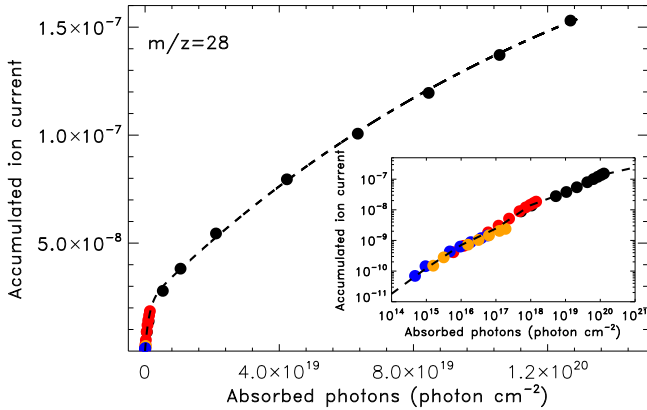


**Figure 5.** Accumulated QMS signal of  $m/z=28$  as a function of absorbed photons during M5 (orange dots), M9 (blue dots), BBw (red dots), and BBs (black dots) experiments. The dashed line is the integral of Equation (1). The inset panel shows the same data in logarithmic scale.

superposition of three exponential functions:

$$Y_{CO} = \frac{\Delta(IC)}{\Delta F_{abs}} = \sum_{i=1}^3 A_i \exp(-\sigma_i F_{abs}) \quad (1)$$

where  $\Delta(IC)$  is the ion current increment over each irradiation step,  $\Delta F_{abs}$  the corresponding number of absorbed photons per  $\text{cm}^2$ , and  $A_i$  and  $\sigma_i$  are the pre-exponential factor and the desorption cross section, respectively. The major sources of error in the estimate of the accumulated ion current are noise and baseline. We perform the sum several times within randomly varying limits, producing a shift and a rotation of

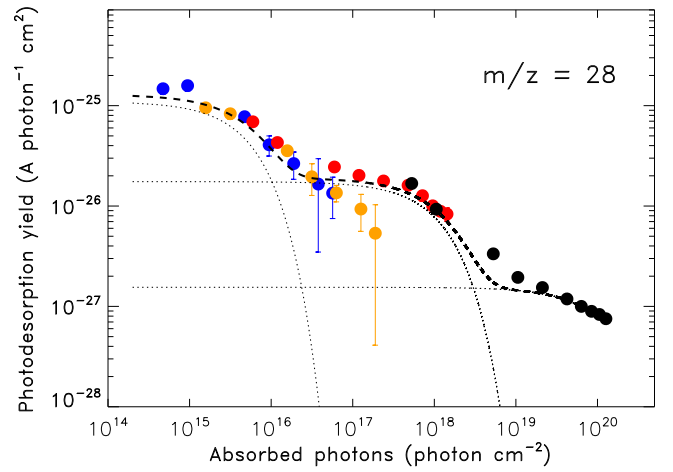


**Figure 6.** Photo-desorption yield vs absorbed photons at each irradiation step for M5 (orange dots), M9 (blue dots), BBw (red dots), and BBs (black dots) experiments. The dashed line corresponds to Equation (1). Dotted lines represent single exponential contributions.

**Table 4**  
Fitting Parameters in Equation (1)

	$A$ ( $A \times \text{cm}^2$ )	$\sigma$ ( $\text{cm}^2$ )
1	$1.0 \times 10^{-25}$	$1.8 \times 10^{-16}$
2	$1.8 \times 10^{-26}$	$8.1 \times 10^{-19}$
3	$1.6 \times 10^{-27}$	$7.0 \times 10^{-21}$

the baseline in either direction. The error on the number of absorbed photons has been chosen to be Poissonian. Such errors have been propagated to obtain a  $3\sigma$  error on the yield,  $Y_{CO}$ . Fitting parameters are reported in Table 4. This relation and its integral are given as dashed lines in Figures 5 and 6, respectively.

Similarly to the ion current, the photo-desorption yield does not depend on the photon rate, although there might be a slight departure from this trend at intermediate photon rates ( $\sim \text{few} \times 10^{12}$ – $\text{few} \times 10^{13}$   $\text{photon s}^{-1}$ ), in the overlapping region ranging from  $10^{16}$  to  $10^{17}$  absorbed photons per square centimeter (see Figure 6).

Since the curvature of the photo-desorption yield changes with the number of absorbed photon (and thus, for each photon rate, with the irradiation time), several photo-desorption channels with different efficiencies might coexist, also giving rise to the modest dispersion at intermediate photon rates reported in Figure 6. To validate this hypothesis, we first investigate if the decrease in the photo-desorption yield is related to specific properties of the icy material such as thickness, composition, and structure variations during the photo-processing.

We initially consider the case of thickness/composition, showing in Figure 7 the CO photo-desorption yield plotted against the CO column density in the ice during the experiments.

The use of CO is imposed by two different constraints on the other two parent molecules, namely an uncertainty in the column density of  $\text{H}_2\text{O}$  where its infrared features overlap with that of  $\text{NH}_3$ , and QMS uncertainties for both  $\text{NH}_3$  and  $\text{H}_2\text{O}$ , who share common fragments ( $m/z=16$  and  $17$ ), thus preventing any accurate determination. It is interesting to note that, while  $Y_{CO}$  decreases by one order of magnitude, the ice

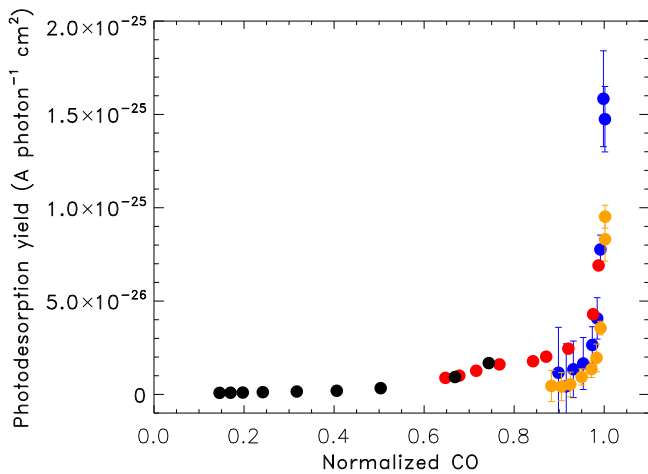


**Figure 7.** Photo-desorption yield of CO plotted against CO column density in the ice. The column density is normalized to its value before processing. Different experiments are labeled as in Figure 5.

CO column density falls at most by 30% depending on the experiment. For instance, during the M5 experiment, the CO column density decreases by only 5%. Considering  $\text{CO}_2$  as the main product, we estimate that during the M5 experiment less than 3% of the deposited CO is ejected into the gas phase. A nonlinear trend is common to all the experiments: this is in sharp contrast to the results of ultraviolet irradiation (Öberg et al. 2007; Muñoz Caro et al. 2010), in which the photo-desorption yield remains constant with the ice thickness up to the very last few monolayers. In addition, pure CO has a poor photochemistry, while the mixture in this paper leads to product formation, which affects the photo-desorption of CO. As X-ray processing continues, the mixture composition changes and therefore also the interactions between molecules; this was not the case in pure CO ices.

The structure of water ices has been extensively studied. The changes in the porosity of solid  $\text{H}_2\text{O}$  induced by thermal processing were analyzed by Bossa et al. (2012), who demonstrated the collapse of the porous structure by increasing the temperature. In addition, thermal desorption differences of  $^{13}\text{CO}$  and  $^{15}\text{N}_2$  have been observed when deposited on compact or porous amorphous solid water (Fayolle et al. 2016), requiring larger desorption temperatures in the amorphous case. In principle, the dangling modes are an indication of either pores in the ice bulk or a rough ice surface topology (e.g., Palumbo 2006; Mejía et al. 2015). However, the absence of dangling bond features in infrared spectra of astrophysical ice analogs, processed thermally or irradiated, does not imply a fully compacted film (Mitchell et al. 2017 and references therein). Raut et al. (2007) studied the compaction of vapor-deposited amorphous solid water by energetic ions at 40 K. They found that the decrease in the strength of the  $-\text{OH}$  dangling features is related to a faster decrease of the surface area of porous ice with respect to the pore volume during irradiation, i.e., the decrease of the pore internal surface area occurs before the collapse of the pore volume. We plot the  $-\text{OH}$  infrared feature at  $3647\text{ cm}^{-1}$  against the photo-desorption yield in Figure 8. We find a milder dependence of  $Y_{\text{CO}}$  on the  $-\text{OH}$  column density with respect to CO column density: for all the experiments, the photo-desorption yield decreases by one order of magnitude when the strength of the dangling  $-\text{OH}$  features in the ice is reduced by at least 30%.

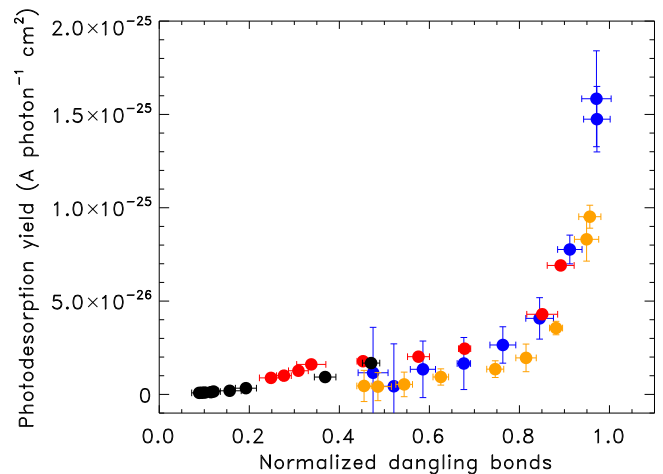


**Figure 8.** Photo-desorption yield of CO vs. the  $-\text{OH}$  dangling bond infrared band at  $3647\text{ cm}^{-1}$ . The band intensity is normalized to its maximum, occurring before the beginning of ice processing. Different experiments are labeled as in Figure 5.

## 5. Discussion

The relation shown in Figure 7 bears a resemblance to the results reported in Bergeld & Chakarov (2006), who performed pulsed laser photo-desorption experiments of a few monolayers of amorphous water ice deposited over graphite and platinum. They found a high increase of the photo-desorbed molecules followed by a fast decay, which disappeared after a few seconds of irradiation. In addition, they observed a limited decrease of the ice coverage. Bergeld & Chakarov speculated that the observed phenomenon might result from multiphoton excitation, leading to formation of excitons in the ice which eventually promote desorption of neutral and ionic species from adsorbed layers of  $\text{H}_2\text{O}$ .

The absorption of X-rays in the ice causes the ejection of energetic electrons, which in turn gives rise to a secondary electron cascade. The interactions of secondary electrons result in ionizations and excitations, i.e., excitons, of the molecules in the solid. In water ice, excitons have energies in the 8–14 eV range, and they can move up to tens of monolayers from the location at which they are generated (McCoustra & Throer 2018). The exciton energy of CO is in the same range as water (the ionization energy is around 14 eV). McCoustra & Throer (2018) show that the electron desorption intensity decreases with increasing thickness of a  $\text{C}_6\text{H}_6$  layer deposited over a water ice, suggesting that water is the major agent in the process. On the other hand, ultraviolet photo-desorption of CO ice is quenched by about one order of magnitude when CO molecules interact with a water ice surface (Bertin et al. 2012). In our experiment the interactions between radiation and ice molecules are mediated by secondary electrons generated in primary photo-absorption events, whose effects are rather similar to those in the interaction with CO and  $\text{H}_2\text{O}$ . Thus, both species should participate in the desorption of weakly bound species. This reflects the very different nature of the interactions of ultraviolet radiation and X-rays with the ice.

In our experiment the whole picture depends on the the X-ray transmission within the ice, with absorption events, which depend on the photon energy, occurring mainly in the bulk of the sample. Excitons generated within the so-called selvedge region are a source of desorption through DIET, in which, e.g., a hot water molecule may escape from the ice after

having inelastically scattered up to the surface. H<sub>2</sub>O may also fragment, giving rise to H and OH, also likely to be hot. Such species may escape directly into the gas phase, or combine with other mobile hydrogen atoms producing H<sub>2</sub> and H<sub>2</sub>O, which in turn may escape. Such scattering events may also efficiently induce the desorption of weakly bound adsorbates at the surface, e.g., H<sub>2</sub>O and CO molecules. In the bulk, exciton relaxation induces the formation of new species through electronic excitation pathways.

The salient points of our results are as follows: (1) the ion current depends on the flux of incoming photons, independently of the photon energies (in the range exploited in this work); (2) the accumulated (over a single irradiation shift) *IC* increases with the number of absorbed photons; (3) the accumulated *IC* profile shows (at least) two regimes, an initial steep rise followed by a slower increase with the number of absorbed photons; (4) the photo-desorption yield *Y* decreases with the number of absorbed photons, and with the photon rate; (5) *Y* changes its curvature a few times in the absorbed photon range used in the experiments; (6) *Y* initially decreases by about one order of magnitude in the face of a very moderate decrease of the CO column density, and then decreases much more slowly; (7) *Y* shows a similar trend when plotted against the –OH infrared feature at 3647 cm<sup>-1</sup> in the ice, although the resulting profile is smoother than in the previous case.

Points (3) and (5) may reflect the presence of different coexistent photo-desorption mechanisms, and/or variations in the structural properties of the ice. The X-ray production of excitons in the selvage provides an efficient desorption mechanism for weakly bound adsorbates at the solid ice surface (substrate-mediated, exciton-promoted desorption; see McCoustra & Throver 2018). Laboratory measurements of electron low-energy irradiation of benzene (weakly) bound to the surface of an amorphous water ice film give an effective desorption cross-section of  $\sim 10^{-15}$  cm<sup>2</sup> (Marchione et al. 2016). This value is consistent with our description of the CO photo-desorption yield at low numbers of absorbed photons,  $\sim 1.8 \times 10^{-16}$  cm<sup>2</sup> (see Table 4). If  $\mathcal{N}_{\text{wb}}$  is the number of weakly bound molecules on the ice surface, the supply of excitons  $\mathcal{N}_{\text{exc}}^*$  provided by X-ray absorption induces a steady desorption of weakly bound molecules until  $\mathcal{N}_{\text{exc}}^* \sim \mathcal{N}_{\text{wb}}$ . At that stage, the substrate-mediated, exciton-promoted desorption yield falls rapidly, leaving a residual tail of species desorbing from the substrate. This desorbing rate is due to both excitons and direct PSD, and/or other kinds of photon-induced fragmentation events. This scenario is supported by the decrease of the photo-desorption yield with the photon rate: if  $\mathcal{N}$  is the number of molecules close to the substrate surface, then

$$Y \sim \frac{\Delta(\mathcal{N}_{\text{wb}} + \mathcal{N})}{\Delta F_{\text{abs}}} \rightarrow \frac{\Delta \mathcal{N}}{\Delta F_{\text{abs}}} \quad (2)$$

as soon as  $\mathcal{N}_{\text{wb}}/\Delta F_{\text{abs}} \rightarrow 0$ . At this stage the photo-desorption cross-section is decreased by about a factor of 20 (see Table 4, second exponential function), consistently with the cross-section for the loss of molecular water from solid water,  $\sim 10^{-17}$  cm<sup>2</sup>, derived by Marchione et al. (2016). This transition occurs when  $F_{\text{abs}} \sim 2 \times 10^{17}$  photons cm<sup>-2</sup>, when a plateau in *Y* occurs until porosity effects, decreasing the surface/volume ratio, produce the ultimate decline of the yield shown in Figure 8. This final transition happens at

$F_{\text{abs}} \sim 2 \times 10^{18}$  photons cm<sup>-2</sup>, corresponding to  $Y \sim 1 \times 10^{-26}$  A photon<sup>-1</sup> cm<sup>2</sup> (see Figure 8).

Finally, we consider the possibility of the contribution of local heating to desorption; when this occurs, the photo-desorption yield cannot be a linear relation to photon flux. Unfortunately, we performed only two different photon flux irradiations with the same ice thickness. However, preliminary results with a pure CO ice show that, within an order of magnitude in photon flux ( $\sim 10^{13}$ – $10^{14}$  photons s<sup>-1</sup>), the photo-desorption yield is directly proportional to photon flux, thus precluding a relevant role for local heating in photo-desorbing the ice sample.

## 6. Conclusions

In this work we study the photo-desorption arising from soft X-ray irradiation of an ice mixture containing water, carbon monoxide, and ammonia (1.5:1.3:1 in ratio). Two distinct regimes apply: an initial phase at low photon fluence in which substrate-mediated, exciton-promoted desorption dominates the photo-desorption yield inducing the release of weakly bound (to the surface) species, followed by the release of species directly from the substrate via exciton-promoted and fragmentation channels, at much higher fluxes. The transition between these two regimes is regulated by the number of weakly bound species.

The present experiment has implications for X-ray photo-desorption in space. On the basis of data provided by the present experiments, we can derive an upper limit to the CO photo-desorption yield. Assuming that the difference between photolyzed CO and new products  $\Delta N_{\text{C}}$  is due to photo-desorption, we may convert the photo-desorption yield (measured in A photon<sup>-1</sup> cm<sup>2</sup>) into a photo-desorption yield in molecules photon<sup>-1</sup>. In the first five minutes of irradiation (thus regarding just the experiments M3, M5, and BBw), CO<sub>2</sub> and HCO are the only C-bearing products observed in the infrared. If we define  $AC^*$  as the accumulated ion current in these initial five minutes of irradiation, we obtain the yield in molecules photon<sup>-1</sup>:

$$Y_{\text{CO}}^{\text{m}} = \left( \frac{\Delta N_{\text{C}}}{AC^*} \right) Y_{\text{CO}} = 9.5 \times 10^{24} Y_{\text{CO}} \quad (3)$$

where  $Y_{\text{CO}}$  is the photo-desorption yield given in Equation (1). The photo-desorption yield in our experiments varies from 1.4 to 0.007 molecules photon<sup>-1</sup> in the range  $\sim 10^{15}$ – $10^{20}$  absorbed photons cm<sup>-2</sup>. For comparison, the photo-desorption yield of CO molecules in a CO ice at 15 K irradiated by ultraviolet is  $\sim 3.5 \times 10^{-2}$  molecules photon<sup>-1</sup> (Muñoz Caro et al. 2010).

Using our results we can simulate the evolution of the photo-desorption yield in a protoplanetary disk, under the assumptions that photo-desorption does not depend on the ice thickness, and that accretion onto the grains is inhibited during the simulation. Inserting Equation (3) in the protoplanetary disk model by Walsh et al. (2012) we simulate the CO X-ray-induced photo-desorption yield in a T Tauri irradiated disk (see Figure 9). The photo-desorption yield is  $\sim 1.2$  molecules photon<sup>-1</sup> in the mid-plane of the disk during the first million years. Interestingly, since the short-lived exciton-promoted desorption phase depends on the intensity of the impinging radiation, after a short transient the photo-desorption yield becomes much weaker in the outer regions of the disk than in the mid-plane.

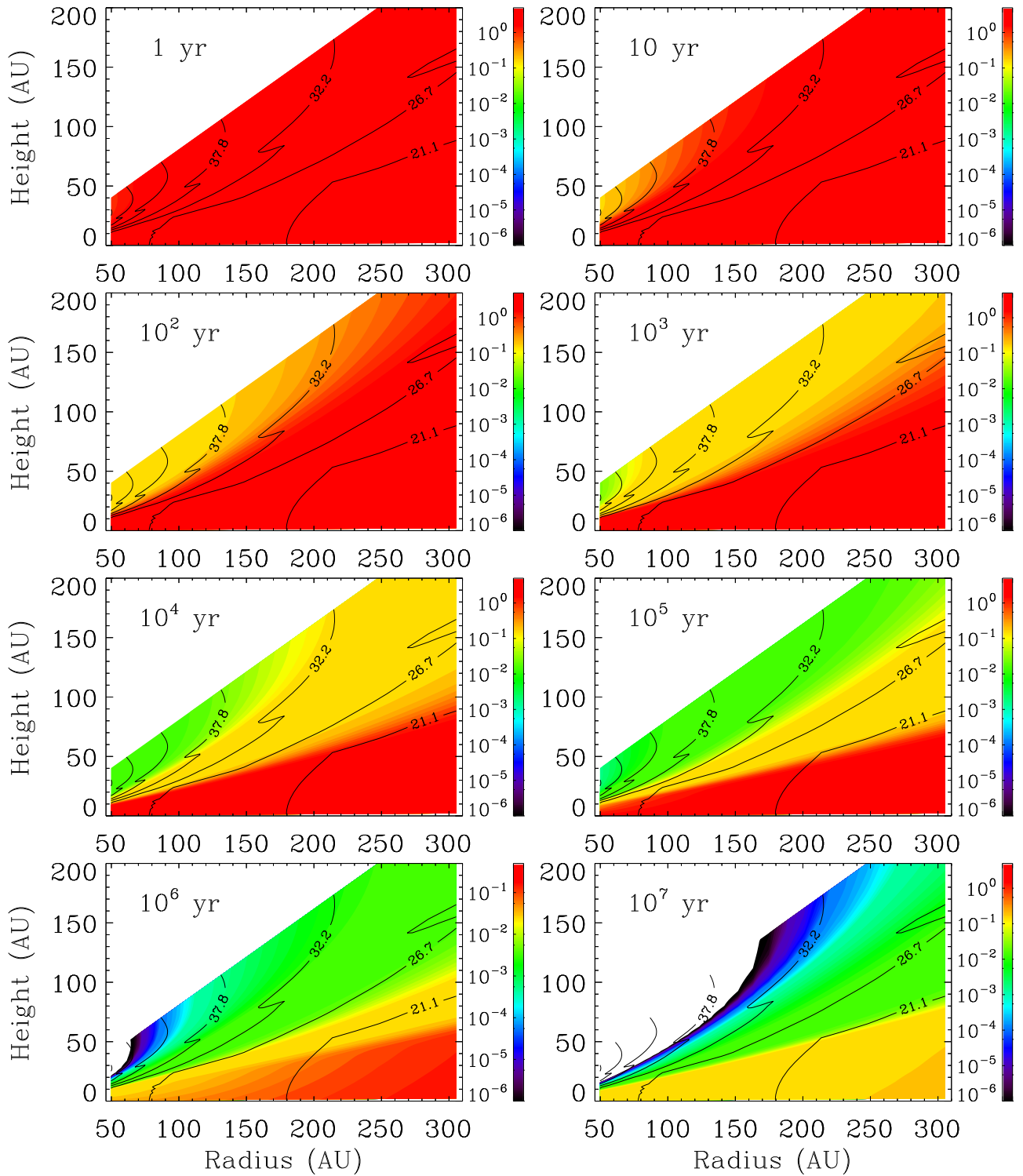


**Figure 9.** Photo-desorption yield of CO in molecules  $\text{photon}^{-1}$  as function of the evolutionary age of a synthetic protoplanetary disk around a classical T Tauri star (Walsh et al. 2012). The photo-desorption yield of CO has been computed assuming the same yield as in the X-ray experiment; see Equation (3).

X-rays may induce sublimation of ice, and therefore desorb molecules from grains, through so-called spot-heating, in which desorption is due to transient heating events (e.g., Najita et al. 2001). In fact, we recorded an enhancement of temperature at the window during the X-ray irradiation. Although the increase in temperature is confined within 1 K,

the effective temperature increase of the system ice/grain may be much higher, as the window is tightly connected to the cryostat. We shall discuss this issue in a future work.

We conclude that X-ray photo-desorption processes should be taken into account in the modeling of protoplanetary disks, and more generally in X-ray-dominated regions.

We acknowledge the NSRRC general staff for running the synchrotron radiation facility. We also thank Dr. T.-W. Pi, the spokesperson of BL08B at the NSRRC.

This work has been supported by the project PRIN-INAF 2016 The Cradle of Life—GENESIS-SKA (General Conditions in Early Planetary Systems for the rise of life with SKA). We also acknowledge support from INAF through the “Progetto Premiale: A Way to Other Worlds” of the Italian Ministry of Education, the MOST grants MOST 107-2112-M-008-016-MY3 (Y-JC), Taiwan, and project AYA-2011-29375, AYA- 2014-60585-P of Spanish MINECO.

### ORCID iDs

A. Jiménez-Escobar  <https://orcid.org/0000-0003-3360-9333>

A. Ciaravella  <https://orcid.org/0000-0002-3127-8078>

C. Cecchi-Pestellini  <https://orcid.org/0000-0001-7480-0324>

Y.-J. Chen  <https://orcid.org/0000-0003-4497-3747>

### References

- Altwegg, K., Balsiger, H., Bar-Nun, A., et al. 2016, *Sci*, **2**, e1600285
- Bergeld, J., & Chakarov, D. 2006, *JChPh*, **125**, 141103
- Bertin, M., Fayolle, E. C., Romanzin, C., et al. 2012, *PCCP*, **14**, 9929
- Boogert, A. C. A., Gerakines, P. A., & Whittet, D. C. B. 2015, *ARA&A*, **53**, 541
- Bossa, J. B., Isokoski, K., de Valois, M. S., & Linnartz, H. 2012, *A&A*, **545**, A82
- Chen, H.-F., Nuevo, M., Chu, C.-C., et al. 2011, *AdSpR*, **47**, 1633
- Chen, Y.-J., Chuang, K.-J., Muñoz Caro, G. M., et al. 2014, *ApJ*, **781**, 15
- Chen, Y.-J., Ciaravella, A., Muñoz Caro, G. M., et al. 2013, *ApJ*, **778**, 162
- Ciaravella, A., Chen, Y.-J., Cecchi-Pestellini, C., et al. 2016, *ApJ*, **819**, 38
- Ciaravella, A., Jimenez Escobar, A., Cecchi-Pestellini, C., et al. 2018, *ApJ*, submitted
- Cruz-Díaz, G. A., Martín-Doménech, R., Muñoz-Caro, G. M., & Chen, Y.-J. 2016, *A&A*, **592**, A68
- Dartois, E., Augé, B., Boduch, P., et al. 2015, *A&A*, **576**, A125
- Fayolle, E. C., Balfe, J., Loomis, R., et al. 2016, *ApJL*, **816**, L28
- Fayolle, E. C., Bertin, M., Romanzin, C., et al. 2011, *ApJL*, **739**, L36
- Fayolle, E. C., Bertin, M., Romanzin, C., et al. 2013, *A&A*, **556**, A122
- Garrod, R. T., Wakelam, V., & Herbst, E. 2007, *A&A*, **467**, 1103
- Gerakines, P. A., Schutte, W. A., Greenberg, J. M., & van Dishoeck, E. F. 1995, *A&A*, **296**, 810
- Goesmann, F., Rosenbauer, H., Bredehöft, J. H., et al. 2015, *Sci*, **349**, aab0689
- Henke, B. L., Gullikson, E. M., & Davis, J. C. 1993, *ADNDT*, **54**, 181
- Jiang, G. J., Person, W. B., & Brown, K. G. 1975, *JChPh*, **64**, 1201
- Jiménez-Escobar, A., Chen, Y.-J., Ciaravella, A., et al. 2016, *ApJ*, **820**, 25
- Jiménez-Escobar, A., Giuliano, B. M., Muñoz Caro, G. M., Cernicharo, J., & Marcelino, N. 2014, *ApJ*, **788**, 19
- Maier, G., Reisenauer, H. P., & Rademacher, K. 1988, *CEJ*, **4**, 1957
- Marchione, D., Thrower, J. D., & McCoustra, M. R. S. 2016, *PCCP*, **18**, 4026
- Martín-Doménech, R., Manzano-Santamaría, J., Muñoz Caro, G. M., et al. 2015, *A&A*, **584**, A14
- Martín-Doménech, R., Muñoz Caro, G. M., & Cruz-Díaz, G. A. 2016, *A&A*, **589**, A107
- McCoustra, M. R. S., & Thrower, J. D. 2018, in *Encyclopedia of Interfacial Chemistry*, ed. K Wandelt (Amsterdam: Elsevier), 383
- Meinert, C., Myrgorodska, I., de Marcellus, P., et al. 2016, *Sci*, **352**, 208
- Mejía, C., de Barros, A. L. F., Seperuelo Duarte, E., et al. 2015, *Icar*, **250**, 222
- Mencos, A., & Krim, L. 2016, *MNRAS*, **460**, 1990
- Mitchell, E. H., Rautt, U., Teolis, B. D., & Baragiola, R. A. 2017, *Icar*, **285**, 291
- Muñoz Caro, G. M., Jiménez-Escobar, A., Martín-Gago, J. Á., et al. 2010, *A&A*, **522**, A108
- Muñoz Caro, G. M., Meierhenrich, U. J., Schutte, W. A., et al. 2002, *Natur*, **416**, 403
- Najita, J., Bergin, E. A., & Ullom, J. N. 2001, *ApJ*, **561**, 880
- Oba, Y., Takano, Y., Watanabe, N., & Kouchi, A. 2016, *ApJL*, **827**, L18
- Öberg, K. I., Fuchs, G. W., Awad, Z., et al. 2007, *ApJL*, **662**, L23
- Palumbo, M. E. 2006, *A&A*, **453**, 903
- Parent, Ph., Laffon, C., Mangeney, C., et al. 2002, *JChPh*, **117**, 10842
- Pilling, S., Seperuelo Duarte, E., da Silveira, E. F., et al. 2010, *A&A*, **509**, A87
- Raut, U., Teolis, B. D., Loeffler, M. J., et al. 2007, *JChPh*, **126**, 244511
- Rawlings, J. M. C., Williams, D. A., Viti, S., Cecchi-Pestellini, C., & Duley, W. W. 2013, *MNRAS*, **430**, 264
- Sandford, S. A., & Allamandola, L. J. 1993, *ApJ*, **417**, 815
- Sekitani, T., Ikenaga, E., Kenichiro, T., et al. 1997, *SurSc*, **390**, 107
- Walsh, C., Nomura, H., Millar, T. J., & Aikawa, Y. 2012, *ApJ*, **747**, 114